












Thermal conductivity measurements of sub-surface buried substrates by steady-state thermoreflectance

Cite as: Rev. Sci. Instrum. **92**, 064906 (2021); <https://doi.org/10.1063/5.0049531>

Submitted: 05 March 2021 . Accepted: 06 June 2021 . Published Online: 29 June 2021

 Md Shafkat Bin Hoque,  Yee Rui Koh,  Kiumars Aryana,  Eric R. Hoglund,  Jeffrey L. Braun, David H. Olson,  John T. Gaskins,  Habib Ahmad, Mirza Mohammad Mahbube Elahi,  Jennifer K. Hite,  Zayd C. Leseman,  W. Alan Doolittle,  Patrick E. Hopkins, et al.



View Online



Export Citation



CrossMark

ARTICLES YOU MAY BE INTERESTED IN

[A steady-state thermoreflectance method to measure thermal conductivity](#)



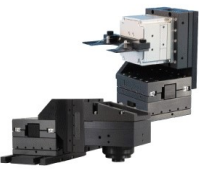
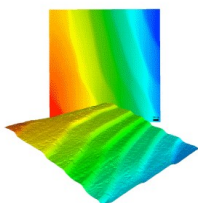
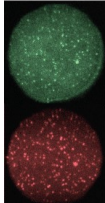
Review of Scientific Instruments **90**, 024905 (2019); <https://doi.org/10.1063/1.5056182>

[Tutorial: Time-domain thermoreflectance \(TDTR\) for thermal property characterization of bulk and thin film materials](#)

Journal of Applied Physics **124**, 161103 (2018); <https://doi.org/10.1063/1.5046944>

[Spatially resolved thermoreflectance techniques for thermal conductivity measurements from the nanoscale to the mesoscale](#)

Journal of Applied Physics **126**, 150901 (2019); <https://doi.org/10.1063/1.5120310>

 MCL MAD CITY LABS INC. www.madcitylabs.com	<p>Nanopositioning Systems</p> 	<p>Modular Motion Control</p> 	<p>AFM and NSOM Instruments</p> 	<p>Single Molecule Microscopes</p> 
---	--	--	---	--

Thermal conductivity measurements of sub-surface buried substrates by steady-state thermoreflectance

Cite as: Rev. Sci. Instrum. 92, 064906 (2021); doi: 10.1063/5.0049531

Submitted: 5 March 2021 • Accepted: 6 June 2021 •

Published Online: 29 June 2021



Md Shafkat Bin Hoque,¹ Yee Rui Koh,¹ Kiumars Aryana,¹ Eric R. Hoglund,² Jeffrey L. Braun,¹ David H. Olson,¹ John T. Gaskins,¹ Habib Ahmad,³ Mirza Mohammad Mahbube Elahi,⁴ Jennifer K. Hite,⁵ Zayd C. Leseman,^{6,7} W. Alan Doolittle,³ and Patrick E. Hopkins^{1,2,8,a)}

AFFILIATIONS

¹ Department of Mechanical and Aerospace Engineering, University of Virginia, Charlottesville, Virginia 22904, USA

² Department of Materials Science and Engineering, University of Virginia, Charlottesville, Virginia 22904, USA

³ School of Electrical and Computer Engineering, Georgia Institute of Technology, Atlanta, Georgia 30332, USA

⁴ Department of Electrical and Computer Engineering, University of New Mexico, Albuquerque, New Mexico 87131, USA

⁵ U.S. Naval Research Laboratory, Washington, DC 20375, USA

⁶ Department of Mechanical Engineering, King Fahd University of Petroleum and Minerals, Dhahran, Eastern Province 31261, Saudi Arabia

⁷ Interdisciplinary Research Center for Advanced Materials, King Fahd University of Petroleum and Minerals, Dhahran, Eastern Province 31261, Saudi Arabia

⁸ Department of Physics, University of Virginia, Charlottesville, Virginia 22904, USA

^{a)} Author to whom correspondence should be addressed: phopkins@virginia.edu

ABSTRACT

Measuring the thermal conductivity of sub-surface buried substrates is of significant practical interests. However, this remains challenging with traditional pump-probe spectroscopies due to their limited thermal penetration depths. Here, we experimentally and numerically investigate the TPD of the recently developed optical pump-probe technique steady-state thermoreflectance (SSTR) and explore its capability for measuring the thermal properties of buried substrates. The conventional definition of the TPD (i.e., the depth at which temperature drops to 1/e value of the maximum surface temperature) does not truly represent the upper limit of how far beneath the surface SSTR can probe. For estimating the uncertainty of SSTR measurements of a buried substrate *a priori*, sensitivity calculations provide the best means. Thus, detailed sensitivity calculations are provided to guide future measurements. Due to the steady-state nature of SSTR, it can measure the thermal conductivity of buried substrates that are traditionally challenging by transient pump-probe techniques, exemplified by measuring three control samples. We also discuss the required criteria for SSTR to isolate the thermal properties of a buried film. Our study establishes SSTR as a suitable technique for thermal characterizations of sub-surface buried substrates in typical device geometries.

Published under an exclusive license by AIP Publishing. <https://doi.org/10.1063/5.0049531>

I. INTRODUCTION

Thin films with thicknesses ranging from nanometer to micrometer length scales have become an integral part of transistors,^{1,2} thermoelectric devices,³ optical coatings,⁴ solar cells,⁵ and memory devices.^{6–8} As the device efficiency and reliability are often dictated by the thermal performance, it is of crucial importance to properly characterize the thermal properties of the

thin films and substrates.⁹ Traditional optical pump-probe and electrothermal methods, such as time-domain thermoreflectance (TDTR),^{10–13} frequency-domain thermoreflectance (FDTR),¹⁴ and the 3ω method,^{15,16} are widely used to measure the thermal conductivity of thin films.¹⁷ However, both TDTR and FDTR have shallow thermal penetration depths (~ 0.2 to $3\ \mu\text{m}$) under standard operating conditions.^{18,19} As a result, they often cannot measure thermal conductivity of buried substrates located beyond these length

scales. The disadvantages of the 3ω method, on the other hand, include its requirement of large and flat sample surface,²⁰ complex microfabrication,²¹ and challenging sample preparation, particularly for electrically conducting and semiconducting materials.¹⁸ These requirements can often limit the applicability of the 3ω method for buried substrate measurements. The recently developed optical pump-probe technique steady-state thermoreflectance (SSTR) offers a solution to these issues as its thermal penetration depth can be much larger than those produced during TDTR and FDTR measurements.^{19,22} In addition, SSTR is well suited for electrically conducting or semiconducting materials and can operate on an optically smooth surface of $100 \times 100 \mu\text{m}^2$ area or less.^{19,23} Therefore, a detailed study into the thermal penetration depth of the SSTR technique and its ability to measure the thermal conductivity of sub-surface buried substrates is highly warranted.

Using the principle of thermoreflectance,²⁴ SSTR employs co-axially focused pump and probe beams from continuous wave (CW) lasers to directly measure the thermal conductivity of a material by applying Fourier's law. Schematics of the SSTR measurement configuration and principle are shown in Figs. 1(a) and 1(b), respectively. Using a low modulation frequency ($f \rightarrow 0$), the pump laser generates a periodic heat flux at the sample surface for an extended period. The low modulation frequency provides enough time for the system to reach steady-state. The probe beam then measures the resultant steady-state temperature rise by monitoring the change in surface reflectivity with a balanced photodetector and a lock-in amplifier. A linear relation between the heat flux and temperature rise is established by varying the pump power and monitoring the resulting change in reflectivity at each pump power. From this relation, the thermal conductivity of any material can be determined by using Fourier's law. The thermal conductivity tensor measured by SSTR is different from that of TDTR or FDTR. For bulk materials, whereas TDTR and FDTR usually measure the cross-plane thermal conductivity, SSTR measures $\sqrt{k_r k_z}$, where k_z and k_r are cross-plane and in-plane thermal conductivities, respectively.¹⁹

In alignment with TDTR and FDTR, in SSTR, the thermal penetration depth (TPD) is defined as the distance normal to the surface

at which the temperature drops to the $1/e$ value of the maximum surface temperature (T_{max}).^{25–28} According to this definition, the $1/e^2$ heater (pump) radius represents the upper limit of the TPD when the modulation frequency is low, such as in SSTR.²⁸ However, such a description of the SSTR TPD fails for multilayer material systems (e.g., a thin film on a substrate). In such systems, the TPD can change widely based on the ratio of thin film to substrate thermal conductivity and the thermal boundary conductance (G) between the thin film and substrate. This is further complicated by the presence of thin metal film transducers at the sample surface, which are often a requirement in optical pump-probe techniques for optothermal transduction.^{29–33}

In this study, we numerically and experimentally analyze the TPD definition of SSTR measurements. We also discuss the implications of metal film transducers, thermal boundary conductances, and role of multilayer material systems on the heuristic approximations for the SSTR TPD. Notably, our experimental results indicate that although the traditional TPD definition provides a convenient estimate of how far beneath the surface SSTR can probe, it does not represent the absolute upper limit of the SSTR probing depth. In specific cases, SSTR can probe beyond both the $1/e$ temperature drop distance and the heater radius. Furthermore, the thermal conductivity measurements of buried layers or substrates by SSTR are not solely dictated by the TPD. The uncertainties associated with such measurements are often governed by the transducer thermal conductivity, the thermal boundary conductances, and the thermal resistances offered by different layers of the multilayer material system. Thus, when determining whether the material of interest at some depth under the surface is measurable within acceptable limits of uncertainty, sensitivity calculations provide the best means. Moreover, we show that due to the application of continuous wave pump laser and low modulation frequency, SSTR can measure the thermal conductivities of buried substrates that are traditionally challenging by TDTR and FDTR. This is illustrated by measuring the thermal conductivities of buried substrates in three different samples: (i) ~ 130 nm amorphous silicon dioxide (a-SiO₂) thin film on a silicon (Si) substrate, (ii) $\sim 2.05 \mu\text{m}$ gallium nitride (GaN) thin film

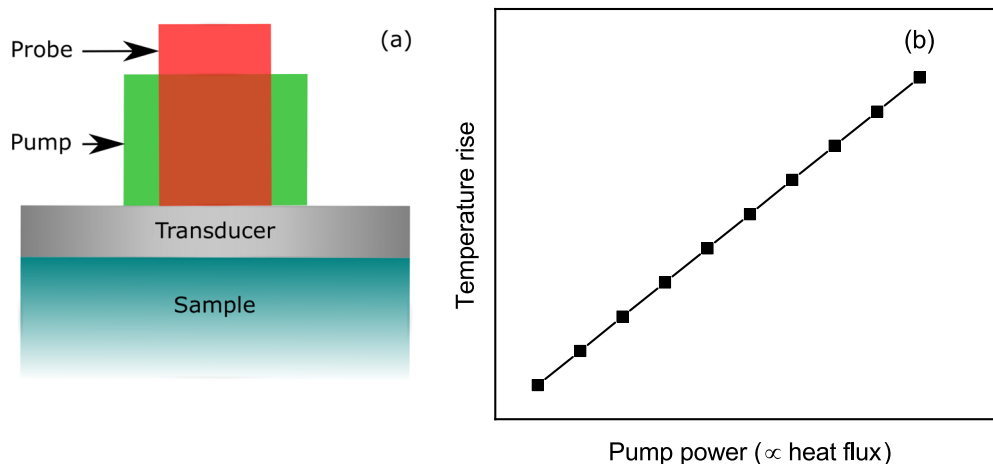


FIG. 1. Schematics of the SSTR measurement: (a) configuration and (b) principle.

on a *n*-type GaN substrate, and (iii) $\sim 2\ \mu\text{m}$ aluminum nitride (AlN) thin film on a sapphire substrate. In addition, it is also established that using large $1/e^2$ pump and probe radii, SSTR can measure the thermal conductivity of highly resistive buried films.

II. RESULTS AND DISCUSSION

We have divided the findings of this study into several sections. The TPD of the SSTR technique is first numerically investigated and then validated by experimental measurements. Section II A presents numerical predictions of SSTR TPD for a two-layer system (metal transducer/substrate), which are then extended to a three-layer system (metal transducer/thin film/substrate) in Sec. II B. This section shows how different ratios of thin film to substrate thermal conductivity can influence the TPD of the SSTR technique. The traditional definition of the thermal penetration depth is experimentally verified in Secs. II C and II D for a three-layer system where both the thin film and substrate are considered to possess the same thermal conductivity. In Sec. II E, experimental measurements of buried substrates for three control samples are presented. The control samples possess different combinations of thin film and substrate thermal conductivities. This is followed by a brief discussion on the required criteria for SSTR measurements of buried films in Sec. II F. To guide future measurements of buried substrates, in Sec. II G, we have presented detailed sensitivity calculations for multiple heater radii and different ratios of thin film to substrate thermal conductivity. A few limitations of the SSTR technique for the measurements of buried films and substrates are discussed in the subsequent Sec. II H.

A. SSTR thermal penetration depth of a two-layer system

We first review how the TPD of SSTR changes as a function of substrate thermal conductivity in a two-layer system: metal transducer/substrate. The substrate here represents a bulk isotropic material. The TPD is calculated by solving the cylindrical heat diffusion equation, detailed descriptions of which are provided elsewhere.²⁶ For these calculations, $1/e^2$ pump and probe radii (r_0 and r_1 ,

respectively) of $10\ \mu\text{m}$ are used. The modulation frequency is chosen to be 100 Hz as it represents a realistic value usable in an experiment. We further assume that all the energy is absorbed in an infinitesimal thin layer on the surface (i.e., surface boundary condition).

In Fig. 2(a), the TPD corresponding to the $1/e$ temperature drop distance from the surface is presented for two scenarios, with and without the inclusion of a transducer. When no transducer is present, the change in the TPD is very small with respect to the substrate thermal conductivity. The small decrease in the TPD with substrate thermal conductivity reduction can be attributed to the choice of modulation frequency. For a given pump and probe radii, the lower the substrate thermal conductivity, the longer it takes for the system to reach steady-state.¹⁹ Thus, as the substrate thermal conductivity decreases, the system slightly deviates from the ideal steady-state condition ($f = 0$). To keep the TPD constant, the modulation frequency needs to be lowered in accordance with the substrate thermal conductivity reduction. However, for the chosen modulation frequency of 100 Hz, the deviation from the ideal steady-state condition is quite small for the substrate thermal conductivities considered here, and therefore, the system can still be reasonably approximated to be in steady-state.¹⁹

The presence of a high thermal conductivity ($100\ \text{W m}^{-1}\text{K}^{-1}$) metallic transducer drastically changes the TPD. For instance, when the substrate thermal conductivity is low ($<10\ \text{W m}^{-1}\text{K}^{-1}$), the TPD with the transducer is higher than the TPD without the transducer. This stems from the radial heat spreading in the transducer and a corresponding increase in the overall heater radius.²⁸ On the other hand, when the substrate thermal conductivity is high ($>100\ \text{W m}^{-1}\text{K}^{-1}$), the TPD with the transducer sharply decreases. With the increase in substrate thermal conductivity, the thermal resistance offered by the probed region gradually decreases. This leads to an increasingly important role of the interfacial thermal resistance. As a result, for high thermal conductivity substrates, the temperature drop at the transducer/substrate interface can become comparable to or even greater than that in the substrate.²⁸ This is exemplified in Fig. 2(b), where we present the normalized temperature drop as a function of depth for a substrate thermal conductivity of $1000\ \text{W m}^{-1}\text{K}^{-1}$. In this example, the temperature decreases by

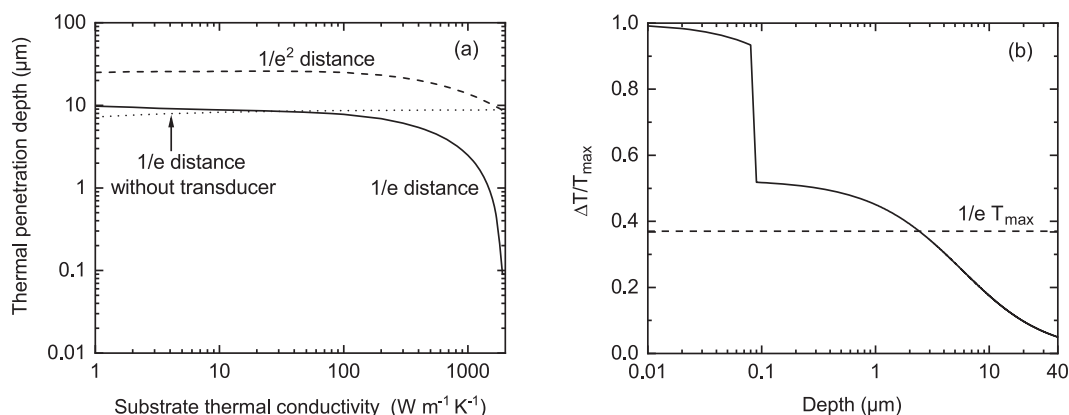


FIG. 2. (a) Thermal penetration depth as a function of substrate thermal conductivity for a two-layer system: metal transducer/substrate. (b) Normalized temperature drop ($\Delta T/T_{\text{max}}$) as a function of depth for a substrate thermal conductivity of $1000\ \text{W m}^{-1}\text{K}^{-1}$. The calculations correspond to $f = 100\ \text{Hz}$, $d_1 = 80\ \text{nm}$, $r_0 = r_1 = 10\ \mu\text{m}$, $k_1 = 100\ \text{W m}^{-1}\text{K}^{-1}$, $C_{V,1} = C_{V,2} = 2\ \text{MJ m}^{-3}\text{K}^{-1}$, and $G_1 = 200\ \text{MW m}^{-2}\text{K}^{-1}$. Here, d and C_V represent thickness and volumetric heat capacity, respectively.

nearly 41% at the transducer/substrate interface, leading to a TPD of $2.48\text{ }\mu\text{m}$.

We also calculate the distance normal to the surface at which the temperature drops to $1/e^2$ value of maximum surface temperature and present it in Fig. 2(a). It is evident that the $1/e^2$ distance (calculated with a transducer) is much higher than the $1/e$ distance for all substrate thermal conductivities. This is to be expected as the temperature decay increases with depth.

B. SSTR thermal penetration depth of a three-layer system

We now extend the TPD discussion to a three-layer system with the following geometry: metal transducer/thin film/substrate. When the thin film and substrate thermal conductivities are nearly equal, the TPD will closely follow those shown in Fig. 2(a) with a minor influence from the thermal boundary conductance between the thin film and substrate. Thus, we consider two extreme cases of this hypothetical geometry: an insulating film on a conductive substrate ($k_2 = 10\text{ W m}^{-1}\text{ K}^{-1}$ and $k_3 = 100\text{ W m}^{-1}\text{ K}^{-1}$) and a conductive film on an insulating substrate ($k_2 = 100\text{ W m}^{-1}\text{ K}^{-1}$ and $k_3 = 10\text{ W m}^{-1}\text{ K}^{-1}$).

In Figs. 3(a) and 3(b), we present the TPD corresponding to the $1/e$ temperature drop distance as a function of thin film thickness for the first and second cases, respectively. It is evident that the TPD with and without presence of a transducer are nearly identical. This is due to the fact that the thin film thermal conductivities are 10 and $100\text{ W m}^{-1}\text{ K}^{-1}$ for the two cases considered here. As shown in Fig. 2(a), for this range of thermal conductivities, the transducer does not have a significant impact on the TPD. Similar to the two-layer system, the $1/e^2$ distance is much higher than the $1/e$ distance in the three-layer system. From Figs. 3(a) and 3(b), it is also clear that the TPD changes greatly with the film thickness when there is a significant difference between thin film and substrate thermal conductivities. Interestingly, the influence of the thin film on the TPD does not subside until the film thickness is approximately four times the heater radius. To understand the rationale behind this, it is necessary to review how the ratio of thin film to substrate thermal conductivity influences the heat flow direction.

In Figs. 3(c) and 3(d), we study the normalized temperature drop as a function of depth for the first and second cases, respectively. When the thin film is insulating and the substrate is conductive, the bulk of the heat flows along the cross-plane direction of the thin film. Due to this, a large temperature gradient exists in the thin film along the cross-plane direction, as shown in Fig. 3(c). Therefore, in this case, the TPD is much lower than the heater radius unless the thin film thickness is too high or too low. On the other hand, when the thin film is conductive and the substrate is insulating, the majority of the heat flows along the in-plane direction of the thin film. Thus, the temperature gradient along the cross-plane direction of the thin film is quite small. As a result, the TPD can be much higher than the heater radius as evident in Fig. 3(d).

To provide a more visual representation of this, the temperature profiles²⁶ of SSTR measurements are shown for a $3\text{ }\mu\text{m}$ thin film corresponding to the first and second cases in Figs. 3(e) and 3(f), respectively. For the insulating thin film case, temperature decreases greatly along the cross-plane direction of the film, whereas for the conductive film case, such a temperature decrease is much smaller.

However, for the conductive thin film case, the temperature decrease is significant along the in-plane direction. This is in alignment with our previous discussion.

C. Experimental verification of the thermal penetration depth definition

Thus far, we have numerically predicted the TPD of two-layer and three-layer systems according to the conventional definition. We now conduct a series of experiments to check the validity of this conventional TPD definition for SSTR measurements. Specifically, we address the following questions: (i) can SSTR probe up to the $1/e$ temperature drop distance defined by the traditional TPD description and (ii) whether this $1/e$ distance or the heater radius represents the absolute upper limit of how deep beneath the surface SSTR can probe?

For this purpose, the thermal conductivities ($\sqrt{k_r k_z}$) of three bulk samples are measured by SSTR: SiO_2 glass, z-cut quartz, and Si. The $1/e$ temperature drop distance of these samples are ~ 10 , 9, and $7\text{ }\mu\text{m}$, respectively, according to the conventional TPD definition presented in Fig. 2(a). Prior to the measurements, the samples are coated with an $\sim 80\text{ nm}$ aluminum (Al) film to serve as an optical transducer. The SSTR experimental proportionality constant, γ ,¹⁹ is determined from a reference sapphire sample ($35 \pm 2\text{ W m}^{-1}\text{ K}^{-1}$).^{34,35} Co-axially focused pump and probe radii of $\sim 10\text{ }\mu\text{m}$ along with a modulation frequency of 100 Hz are used for these SSTR measurements. To minimize measurement noise at this low modulation frequency, we use a combination of factors including a balanced photodetector with a path-matched reference beam, equivalent powers of the reference and sample beams, high-quality laser diodes, low probe power, high pump power, and longer averaging and lock-in times. With the optimum settings of each of these parameters, a signal-to-noise ratio up to 100 can be obtained in our setup.¹⁹ Details of our SSTR setup and measurement procedure have been thoroughly discussed in previous publications.^{19,36}

The SSTR best-fit curves for the thermal conductivities of the three samples are shown in Fig. 4(a). The SSTR-measured thermal conductivities of the SiO_2 glass, z-cut quartz, and Si are 1.14 ± 0.16 , 8.87 ± 0.64 , and $141 \pm 10\text{ W m}^{-1}\text{ K}^{-1}$, respectively. The uncertainties of the measured values stem from the uncertainty associated with the γ value (sapphire reference), Al transducer thermal conductivity, and the thermal boundary conductance. Details of these parameters are listed in Table 1. The measured thermal conductivities of the three specimen are in agreement with the literature.^{12,19,44–46}

In Fig. 4(b), the SiO_2 glass, z-cut quartz, and Si samples are approximated as a three-layer material system: Al transducer/second layer/third layer. Here, the second and third layers represent the thin film and buried substrate of the same material, respectively. We fit for the thermal conductivity of the third layer, assuming that the second layer possesses the value presented in Fig. 4(a). The thermal boundary conductance between the second and third layers is kept fixed at $1000\text{ MW m}^{-2}\text{ K}^{-1}$. Figure 4(b) shows that with the increase in the second layer thickness, the uncertainty of the third layer thermal conductivity increases. When the second layer thickness is equal to the $1/e$ distance (~ 10 , 9, and $7\text{ }\mu\text{m}$ for SiO_2 glass, z-cut quartz, and Si, respectively), the third layer thermal conductivities are 1.15 ± 0.71 , 8.88 ± 2.74 , and

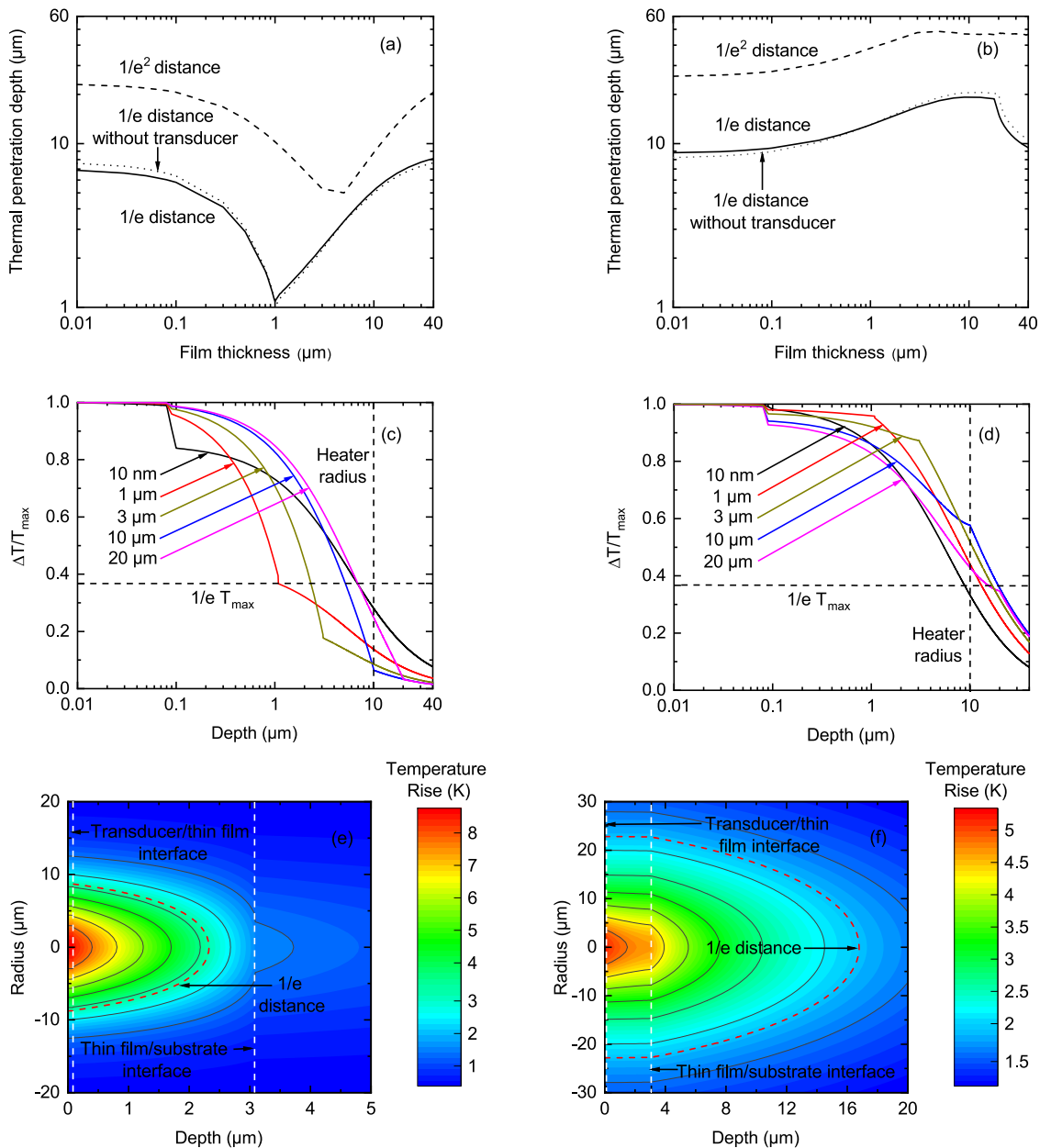


FIG. 3. (a) and (b) Thermal penetration depth as a function of film thickness for a three-layer system: metal transducer/thin film/substrate. (c) and (d) Normalized temperature drop as a function of depth for five different thin film thicknesses. (e) and (f) Temperature profiles of SSTR measurements for a 3 μm thin film on a substrate corresponding to an absorbed power of 5 mW. Panels (a), (c), and (e) represent the case of an insulating film on a conductive substrate ($k_2 = 10 \text{ W m}^{-1} \text{ K}^{-1}$ and $k_3 = 100 \text{ W m}^{-1} \text{ K}^{-1}$), whereas panels (b), (d), and (f) represent the case of a conductive film on an insulating substrate ($k_2 = 100 \text{ W m}^{-1} \text{ K}^{-1}$ and $k_3 = 10 \text{ W m}^{-1} \text{ K}^{-1}$). The calculations correspond to $f = 100 \text{ Hz}$, $d_1 = 80 \text{ nm}$, $r_0 = r_1 = 10 \mu\text{m}$, $k_1 = 100 \text{ W m}^{-1} \text{ K}^{-1}$, $C_{V,1} = C_{V,2} = C_{V,3} = 2 \text{ MJ m}^{-3} \text{ K}^{-1}$, and $G_1 = G_2 = 200 \text{ MW m}^{-2} \text{ K}^{-1}$.

$142.5 \pm 33.7 \text{ W m}^{-1} \text{ K}^{-1}$, respectively. Furthermore, when the second layer thickness is 14 μm , the third layer thermal conductivities are $\sim 1.16 \pm 1.11$, 8.89 ± 4.35 , and $142.7 \pm 61 \text{ W m}^{-1} \text{ K}^{-1}$, respectively.

It is possible to answer the previously posed questions from Fig. 4(b). As shown in this figure, SSTR can measure the thermal

conductivities of layers located at $1/e$ temperature drop distance although such measurements have relatively large uncertainty. However, it is also evident that SSTR can probe beyond this conventional $1/e$ distance and the heater radius. This indicates that immediately beyond the $1/e$ distance or the heater radius, SSTR measurement sensitivity does not drop to zero. This phenomenon can be explained

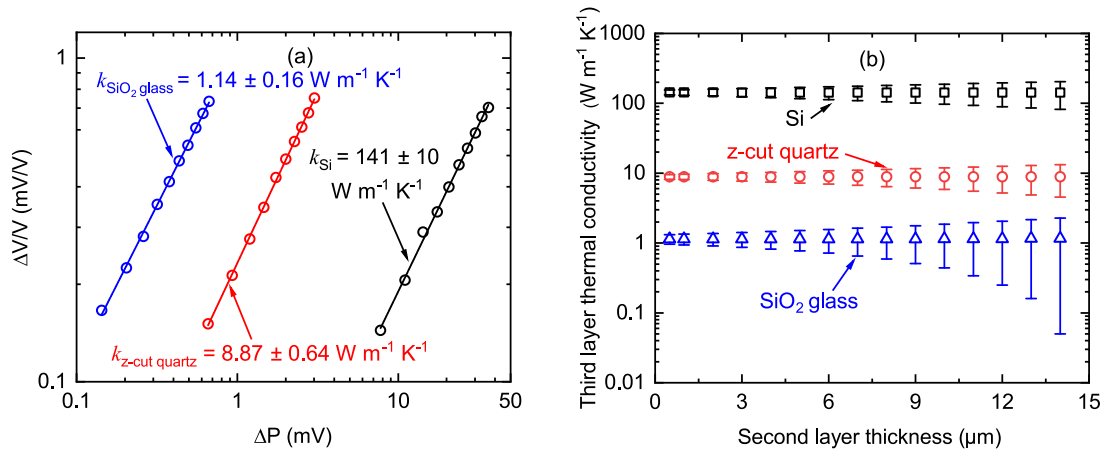


FIG. 4. (a) Probe photodetector response, $\Delta V/V$ (\propto temperature rise), as a function of pump photodetector response, ΔP (\propto pump power), for SSTR fitting of Al coated bulk SiO₂ glass, z-cut quartz, and Si. (b) Third layer thermal conductivity as a function of second layer thickness when the three samples are fitted as a three-layer system: Al transducer/second layer/third layer.

by reviewing Fig. 2(a), which shows that the temperature does not drop to the $1/e^2$ value of the maximum surface temperature until the distance is much higher than the $1/e$ distance or the heater radius. Thus, even though the traditional TPD definition can be used as a convenient estimate of SSTR probing depth, neither the $1/e$ distance nor the heater radius should be taken as an absolute upper limit of how far beneath the surface SSTR can probe. Figure 4(b) also shows

that at the $1/e$ temperature drop distance, the uncertainty associated with the third layer thermal conductivity varies widely among the measured samples. This can be attributed to the fact that SSTR measurements of buried substrates are not solely dictated by the TPD. Therefore, the uncertainty associated with such measurements cannot be estimated from the TPD alone. This is discussed in more detail in Sec. II D.

TABLE I. Parameters used in the SSTR measurements and sensitivity calculations.

Samples	Layers ^a	Thermal conductivity ^b ($\text{W m}^{-1} \text{ K}^{-1}$)	Thermal boundary conductance ^c ($\text{MW m}^{-2} \text{ K}^{-1}$)	
			G_1	G_2
Al/SiO ₂ glass	Al	126 ± 13	150 ± 20	...
Al/quartz	Al	108 ± 12	230 ± 30	...
Al/Si	Al	117 ± 12	180 ± 30	...
Al/130 nm SiO ₂ /Si	Al	180 ± 18	230 ± 50	...
	SiO ₂ ^d	1.35 ± 0.11	...	230 ± 50
Al/2.05 μm GaN/GaN	Al	130 ± 13	240 ± 40	...
	GaN	184 ± 15	...	150 ± 50
Al/2 μm AlN/sapphire	Al	190 ± 19	380 ± 80	...
	AlN	281 ± 26	...	150 ± 50
Al/2.5 μm Si/1 μm SiO ₂ /Si	Al	180 ± 18	100 ± 10	...
	Si	127 ± 11	...	230 ± 50 ^e

^aThe thicknesses of the layers are measured by picosecond acoustics and transmission electron microscopy (TEM). The uncertainties associated with layer thicknesses are about $\sim 2\%$ to 3% .

^bThe thermal conductivities of the Al transducers are measured by the four-point probe. The SiO₂, GaN, AlN, and Si thin film thermal conductivities are measured by TDTR using a modulation frequency of 8.4 MHz. A detailed description of our TDTR setup has been provided elsewhere.^{37,38}

^c G_1 is measured by TDTR. G_2 is estimated from the related literature.^{39–43} As SSTR has negligible sensitivity to G_2 for typical sample configurations, the estimated values do not have an appreciable influence on SSTR measurements.

^dIn the Al/SiO₂ glass sample, the SiO₂ substrate is a commercial glass slide, whereas in the Al/130 nm SiO₂/Si sample, the SiO₂ thin film is laboratory grade SiO₂ grown via dry oxidation.⁴⁰ As a result, the thermal conductivity of SiO₂ is different between the two samples.

^eFor the Al/2.5 μm Si/1 μm SiO₂/Si sample, the thermal boundary conductances of the Si/SiO₂ (G_2) and SiO₂/Si (G_3) interfaces are considered to be the same.

D. Influence of multilayer material systems on the thermal conductivity measurements of buried substrates

To empirically study how different parameters of multilayer material systems impact the thermal conductivity measurements of buried layers or substrates, we use the same examples used in Sec. II C. Figure 5(a) shows the % uncertainty of the third layer thermal conductivity as a function of the second layer thickness corresponding to Fig. 4(b). The uncertainty of the third layer thermal conductivity is highest for SiO₂ glass, followed by z-cut quartz and Si. This may seem counterintuitive as SiO₂ glass has the highest $1/e$ temperature drop distance among the three materials. Thus, one might expect the third layer of the SiO₂ glass to have the lowest uncertainty among the samples. To understand this apparent anomaly, it is necessary to review how sensitivities to different parameters influence the SSTR measurements of third layer thermal conductivity.

The sensitivities of SSTR measurements to different parameters for SiO₂ glass, z-cut quartz, and Si are presented in Figs. 5(b)–5(d), respectively. It is evident from these sensitivity calculations that when the second layer thickness is high, measurements of the third layer are greatly impacted by the second layer thermal conductivity. However, for SiO₂ glass, there is also significant sensitivity to the transducer thermal conductivity, whereas for z-cut quartz and Si, sensitivity to nearly all other parameters is very small. Due to

the influence of second layer and transducer thermal conductivity, the uncertainty of SiO₂ glass is highest. For similar reasons, the uncertainty of the third layer thermal conductivity is higher for z-cut quartz compared to Si when the second layer thickness is high. At such thicknesses, SSTR measurements of z-cut quartz become sensitive to the transducer thermal conductivity. Although Si measurements also become sensitive to the Al/Si interface conductance, the sensitivity of Si to this thermal boundary conductance is lower compared to the sensitivity of z-cut quartz to the transducer thermal conductivity. As a result, the uncertainties of Si measurements are relatively lower than z-cut quartz at high second layer thicknesses.

From the above discussion, it can be concluded that the TPD cannot provide an estimation of the uncertainty associated with SSTR measurements of a buried substrate. Instead, such uncertainty depends on how sensitive SSTR measurements are to different parameters, such as the transducer thermal conductivity, the thermal boundary conductances, and the thermal resistances of different layers of the multilayer material system. Therefore, sensitivity calculations can provide the best means for estimating the uncertainty of a buried layer or substrate thermal conductivity.

E. Experimental measurements of the thermal conductivity of buried substrates by SSTR

To further demonstrate the ability of SSTR to measure the thermal conductivity ($\sqrt{k_r k_z}$) of buried substrates, we choose three

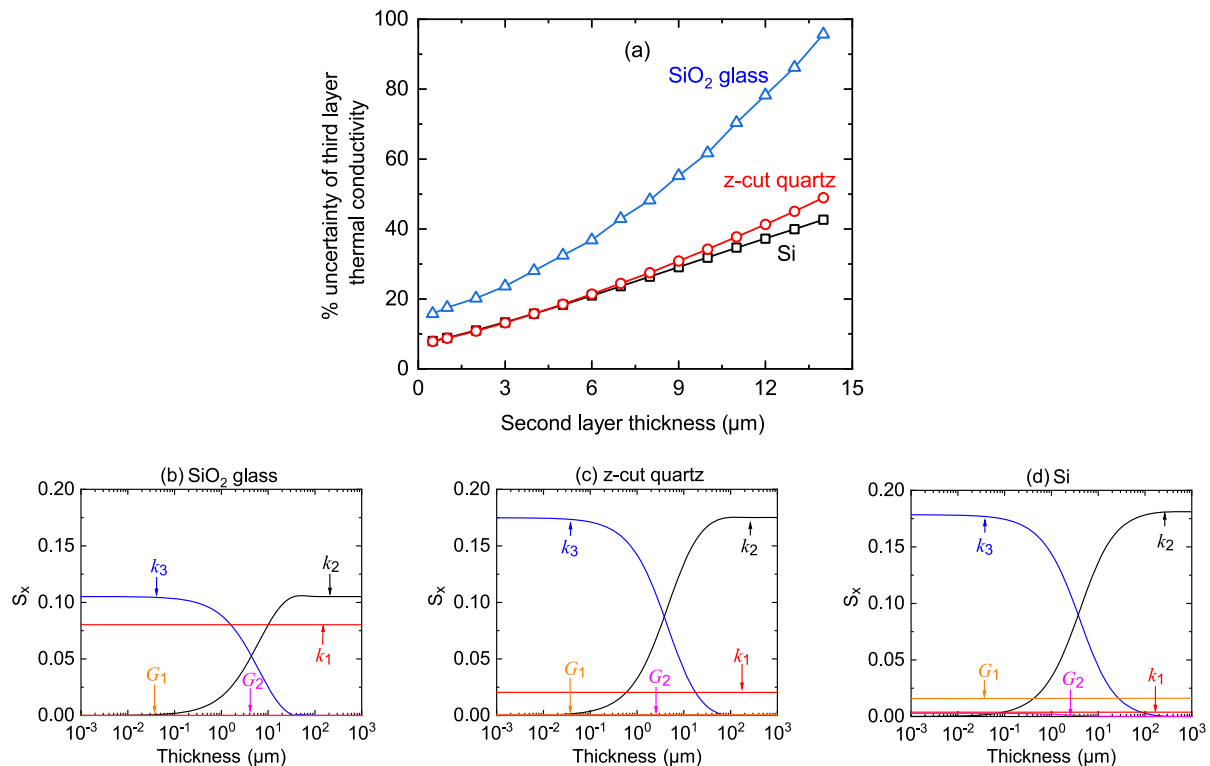


FIG. 5. (a) % uncertainty of the third layer thermal conductivity as a function of second layer thickness corresponding to Fig. 4(b). The sensitivity, S_x , as a function of second layer thickness for (b) SiO₂ glass, (c) z-cut quartz, and (d) Si. For all specimen, k represents $\sqrt{k_r k_z}$.

samples with the following three-layer geometry: Al transducer/thin film/substrate. In these samples, the thin film and substrate are separated by a physical interface contrary to those of Sec. II C. The schematics of the three samples are shown in Figs. 6(a)–6(c). The first sample is a ~ 130 nm a-SiO_2 thin film on the Si substrate. This sample represents an insulating film on a conductive substrate. The second sample is a ~ 2.05 μm unintentional doped (UID) GaN thin film on the hydride vapor phase epitaxy (HVPE) n -GaN substrate. This sample represents the case where the thin film and substrate thermal conductivities are nearly equal. The third sample is a ~ 2 μm molecular beam epitaxy (MBE) grown AlN thin film on the sapphire substrate. This sample represents a conductive film on an insulating substrate. Under standard operating conditions, it is often challenging to measure the thermal conductivity of such buried substrates by TDTR and FDTR due to their limited thermal penetration depths.

In the ~ 130 nm a-SiO_2 thin film on the Si sample, we use co-axially focused $1/e^2$ pump and probe radii of ~ 10 μm to measure the thermal conductivity of the buried Si substrate. The sensitivity calculation for this sample is shown in Fig. 6(d). As shown here, SSTR measurements of the Si substrate are sensitive to the cross-plane thermal conductivity of the SiO_2 thin film. TDTR is used to measure the cross-plane thermal conductivity of the SiO_2 thin film. Using this SiO_2 value as an input, the SSTR-measured thermal conductivity of the Si substrate is 141 ± 27 $\text{W m}^{-1} \text{K}^{-1}$. Figure 6(d) indicates that the sensitivity to SiO_2 cross-plane thermal conductivity is very high when the pump and probe radii are 10 μm . As a result, the uncertainty associated with the Si thermal conductivity is also high, $\sim 19\%$.

The sensitivity calculation also shows that using larger spot sizes, the sensitivity to SiO_2 and corresponding uncertainty of Si measurement can be reduced. To demonstrate this, we repeat the measurement with $1/e^2$ pump and probe radii of ~ 20 μm . The resultant Si thermal conductivity is 140 ± 18 $\text{W m}^{-1} \text{K}^{-1}$. As predicted, the measurement with the 20 μm spot sizes has a reduced uncertainty of $\sim 13\%$.

In the ~ 2.05 μm GaN thin film on the n -GaN substrate sample, we measure the thermal conductivity of the n -GaN substrate by SSTR using ~ 10 and 20 μm spot sizes. GaN samples of similar geometries have received significant attention in recent years for thermal management applications of high-power and high-frequency electronic devices.^{47–51} The sensitivity calculation for our sample is presented in Fig. 6(e). The sensitivities to the in-plane and cross-plane thermal conductivities of the GaN thin film are considerably lower when the spot sizes are 20 μm compared to the 10 μm spot sizes. The cross-plane thermal conductivities of the GaN thin film is measured by TDTR. At room temperature, the in-plane and cross-plane thermal conductivities of the GaN thin film can be considered to be the same.⁵² The SSTR-measured thermal conductivity of the GaN substrate is 194 ± 27 $\text{W m}^{-1} \text{K}^{-1}$ when the spot sizes are 10 μm . Using spot sizes of 20 μm , the thermal conductivity of the GaN substrate is measured with a lower uncertainty to be 185 ± 16 $\text{W m}^{-1} \text{K}^{-1}$.

The thermal conductivity of the sapphire substrate is measured by SSTR in the ~ 2 μm AlN thin film on the sapphire sample. The sensitivity calculation for this sample is shown in Fig. 6(f). SSTR measurement of the sapphire substrate thermal conductivity is most sensitive to the in-plane thermal conductivity of the AlN thin film.

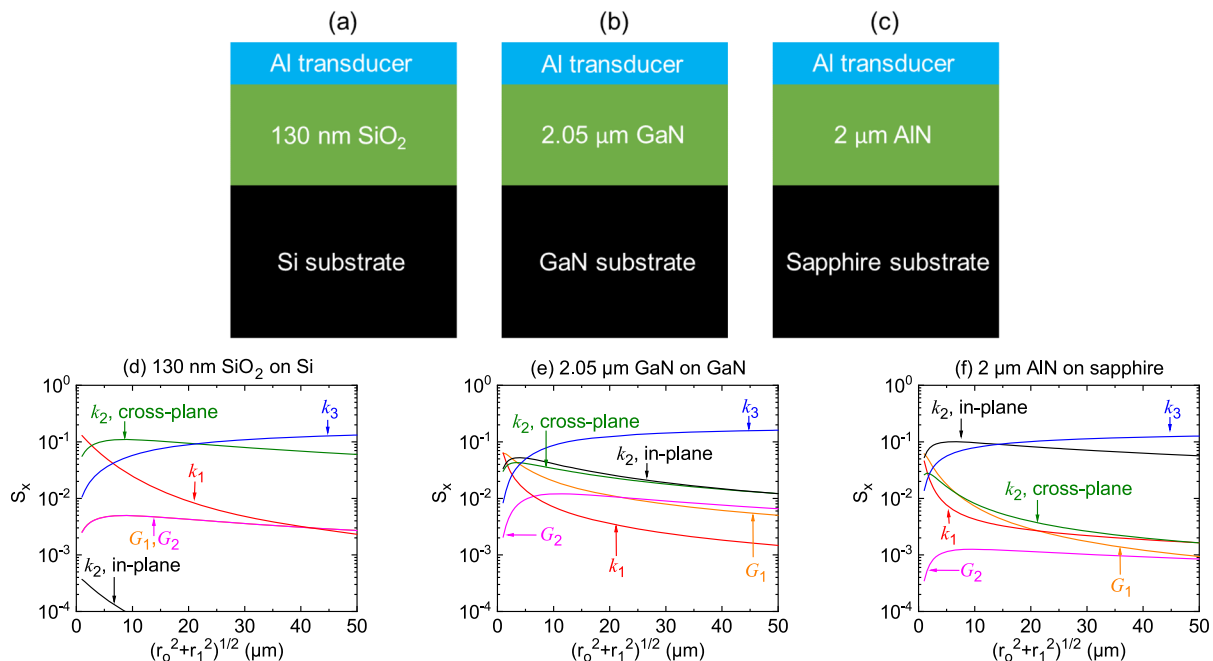


FIG. 6. Schematics of the three-layer samples measured by SSTR: (a) ~ 130 nm SiO_2 thin film on the Si substrate, (b) ~ 2.05 μm GaN thin film on the n -GaN substrate, and (c) ~ 2 μm AlN thin film on the sapphire substrate. Panels (d)–(f) represent the sensitivity calculations as a function of effective radius $\sqrt{r_o^2 + r_1^2}$ for the three samples shown in panels (a)–(c), respectively.

TABLE II. SSTR- and TDTR-measured substrate thermal conductivity of the samples shown in Fig. 6.

Substrates	Thermal conductivity (W m ⁻¹ K ⁻¹)			
	SSTR		TDTR	Literature
	Spot size 10 μm	Spot size 20 μm		
Si	141 ± 27	140 ± 18	132 ± 32	140 ⁴⁴
GaN	194 ± 27	185 ± 16	213 ± 60	195 ⁵³
Sapphire	35.1 ± 5.9	34.5 ± 4.2	36.4 ± 13.5	35 ⁵⁴

The cross-plane thermal conductivity of this AlN thin film is measured by TDTR. As the anisotropy in the AlN thermal conductivity of is very small at room temperature,⁵⁵ the in-plane and cross-plane thermal conductivities of the $2 \mu\text{m}$ AlN thin film can be assumed to be the same. Using SSTR, the thermal conductivity of the sapphire substrate is measured to be $35.1 \pm 5.9 \text{ W m}^{-1} \text{K}^{-1}$ with $1/e^2$ pump and probe radii of $10 \mu\text{m}$. Similar to the other two samples, with $20 \mu\text{m}$ spot sizes, the sapphire thermal conductivity can be determined with a lower uncertainty, $34.5 \pm 4.2 \text{ W m}^{-1} \text{K}^{-1}$.

In Table II, we present the SSTR-measured substrate thermal conductivities for the two spot sizes. The uncertainties of the measured values incorporate the uncertainty associated with the γ value (sapphire reference), Al transducer and thin film thermal conductivities, thin film thickness, and the thermal boundary conductances. The values of these parameters are tabulated in Table I. As shown in Table II, the measured substrate thermal conductivities are in excellent agreement with the literature.

For comparison, we also measure the substrate thermal conductivities with TDTR. These substrates are inaccessible with the typical modulation frequency (~ 8 to 10 MHz) used in TDTR setups.^{38,56–59} Therefore, to enable these measurements, we use a low modulation frequency of 1 MHz . Even with this low modulation frequency, the TDTR TPD^{22,25,26} is much lower than that of SSTR. As a result, the uncertainties associated with the TDTR measurements are significantly higher compared to SSTR as evident in Table II. This proves the superiority of SSTR for accurately measuring the thermal conductivity of sub-surface buried substrates.

F. Experimental measurement of the thermal conductivity of buried films by SSTR

We now discuss the required criteria for SSTR to measure the thermal conductivity of a buried film in a four-layer system: metal transducer/thin film/buried film/substrate. The measurement of such a buried film is possible when the thermal resistance of this layer is much greater than those of the top thin film and substrate. This stems from the fact that for SSTR to measure the thermal conductivity of any layer in a multilayered material system, a significant steady-state temperature gradient must exist in that layer, either in the cross-plane or in-plane direction. As the top thin film is in contact with the metal transducer, the temperature gradient of this layer is often large unless the film thickness is very low. On the other hand, since the substrate is a semi-infinite medium, a measurable temperature gradient exists in the substrate when large pump and probe radii are used. For a buried film, however, unless the thermal resistance is large, the resulting temperature gradient is relatively small

compared to those of the thin film and substrate. Therefore, although SSTR probes through the buried film and is influenced by the thermal properties of this layer, the degree of such influence is relatively small. As a result, SSTR cannot isolate the thermal conductivity of a buried film with low thermal resistance.

In addition, large pump and probe radii ($>10 \mu\text{m}$) are needed for buried film measurements. When the thermal resistance of the buried layer is much higher than those of thin film and substrate, bulk of the heat flows along the in-plane direction of the top thin film. For a sufficient thermal gradient to exist in the buried film, large spot sizes are required.

To experimentally show this, we have selected a sample that fits this criteria: $85 \text{ nm Al transducer}/2.5 \mu\text{m Si film}/1 \mu\text{m SiO}_2 \text{ layer}/\text{Si substrate}$. The sensitivity calculation for this sample is shown in Fig. 7. As exhibited here, SSTR can measure the thermal conductivity of the buried SiO_2 layer when large spot sizes are used. However, such measurements are also sensitive to the in-plane thermal conductivity of the top Si film. TDTR is used to measure the cross-plane thermal conductivity of the top Si film, as shown in Table I. The in-plane and cross-plane thermal conductivities of the $2.5 \mu\text{m}$ Si film can be considered to be the same.⁶⁰ Using $1/e^2$ pump and probe radii of $\sim 20 \mu\text{m}$, we measure the buried SiO_2 film thermal conductivity to be $1.34 \pm 0.26 \text{ W m}^{-1} \text{K}^{-1}$. This value is in agreement with the literature,^{38,61} showing the capability of SSTR to measure the thermal conductivity of sub-surface buried layers.

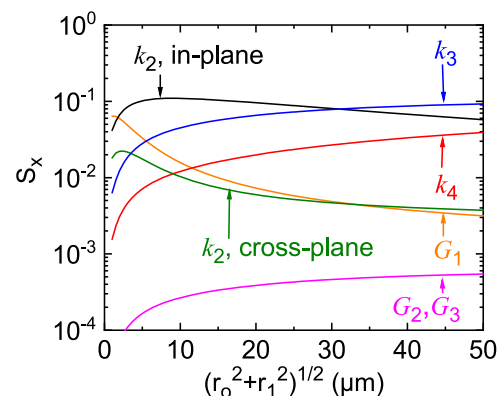


FIG. 7. Sensitivity calculation as a function of effective radius $\sqrt{r_o^2 + r_1^2}$ for the four-layer sample: $85 \text{ nm Al transducer}/2.5 \mu\text{m Si film}/1 \mu\text{m SiO}_2 \text{ layer}/\text{Si substrate}$.

G. Sensitivity calculations to guide future measurements of buried substrates by SSTR

In Fig. 8, we have provided detailed sensitivity calculations for a three-layer system: metal transducer/thin film/substrate corresponding to three different heater radii: 2, 20, and 50 μm . For these calculations, the thin film thermal conductivity is kept fixed at $10 \text{ W m}^{-1} \text{ K}^{-1}$, whereas the substrate thermal conductivity is varied from 1 to $100 \text{ W m}^{-1} \text{ K}^{-1}$. Thus, the first, second, and third columns of Fig. 8 represent thin film to substrate thermal conductivity ratios of 10, 1, and 0.1, respectively. As exhibited here, SSTR measurements are most sensitive to the substrate thermal conductivity when the heater radius is much larger than the thin film thickness, regardless of what the thin film to substrate thermal conductivity ratio is. When the heater radius is small (e.g., 2 μm), the sensitivities to the in-plane and cross-plane thermal conductivities of the substrate are nearly the same. However, as the heater radius increases, sensitivity to the in-plane thermal conductivity of the substrate keeps decreasing. This occurs because larger heater radius requires longer time to reach steady-state. Therefore, to increase the sensitivity to the in-plane thermal conductivity of

the substrate, the modulation frequency needs to be lowered. From Fig. 8, it is evident that by changing the heater radius, it is possible to measure the thermal conductivity of buried substrates for different thin film thicknesses. This figure also shows that with the increase in heater radius, sensitivity to the substrate thermal conductivity continuously increases, while sensitivity to all other parameters decreases. Thus, it can be concluded that using a larger spot size (e.g., 20 or 50 μm), the uncertainty associated with any buried substrate measurement can be reduced. This conclusion is applicable to all the thermal conductivity measurements presented in Secs. II C and II E.

H. Limitations of SSTR for buried film and substrate measurements

The measurements presented in this study establishes SSTR as a suitable technique for measuring buried substrates and buried films in typical device geometries. However, there are a few scenarios where such measurements can become challenging. One such example is when the interfacial resistance between the thin film and substrate is very high (i.e., $200 \text{ m}^2 \text{ K GW}^{-1}$ or greater). In this case, SSTR

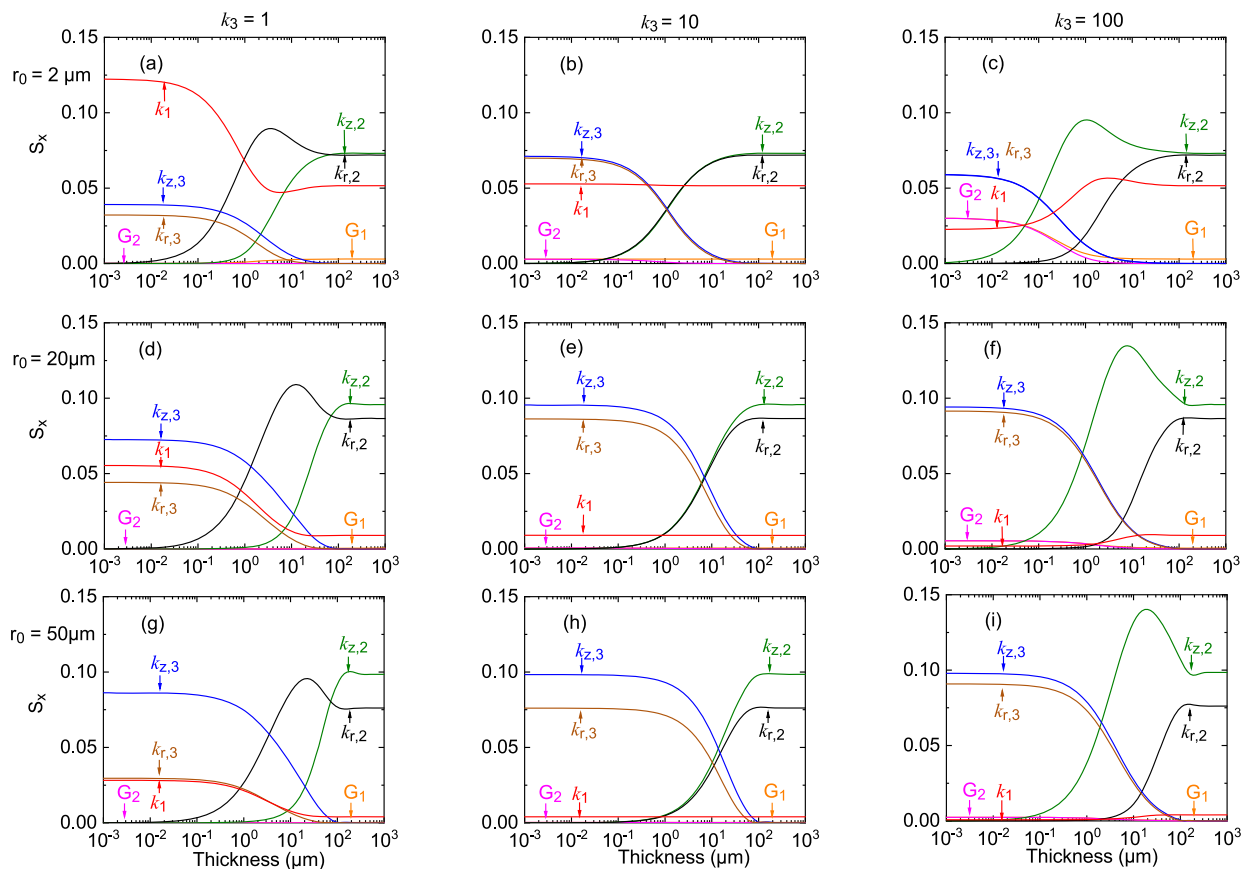


FIG. 8. (a)–(i) Sensitivity, S_x , as a function of thin film thickness for a three-layer system: metal transducer/thin film/substrate. Three different heater radii (r_0) are considered here: 2, 20, and 50 μm . The first, second, and third columns correspond to thin film to substrate thermal conductivity ratios of 10, 1, and 0.1, respectively. The sensitivity calculations correspond to $f = 100 \text{ Hz}$, $d_1 = 80 \text{ nm}$, $r_1 = r_0$, $k_1 = 100 \text{ W m}^{-1} \text{ K}^{-1}$, $C_{V,1} = C_{V,2} = C_{V,3} = 2 \text{ MJ m}^{-3} \text{ K}^{-1}$, $G_1 = G_2 = 200 \text{ MW m}^{-2} \text{ K}^{-1}$, and $k_2 = 10 \text{ W m}^{-1} \text{ K}^{-1}$.

measurements have reduced sensitivity to the buried substrate, and therefore, the resulting uncertainty can be large. However, this also opens up new opportunities for SSTTR. When the interface is highly resistive, the temperature drop at the interface becomes quite large. As SSTTR fundamentally measures the steady-state temperature difference across an interface, for this case, SSTTR becomes sensitive to the interfacial thermal resistance between the thin film and substrate. Buried interfaces are also known to be challenging. Measurements of such highly resistive buried interfaces might be of interest for a future study.

Similarly, if the thermal boundary conductance between the Al transducer and thin film is very low, SSTTR measurements become sensitive to this interfacial resistance. As a result, sensitivity to other parameters reduces.

In addition, as discussed in Sec. II F, SSTTR can isolate the thermal conductivity of a buried layer when the resistance offered by this layer is much higher than those of the top film and substrate. Therefore, if the buried film is conductive, then it is not possible to measure the thermal conductivity of the film with SSTTR.

Despite these limitations, SSTTR technique demonstrates significant advantages in buried film and substrate measurements compared to the traditional pump-probe techniques.

III. CONCLUSION

We experimentally and numerically investigate the influences of multilayer material systems, thin metal film transducers, and thermal boundary conductances on the TPD of the SSTTR technique. The traditional TPD definition of the $1/e$ temperature drop distance from the maximum surface temperature does not represent the absolute upper limit of the SSTTR probing depth. Thus, when estimating whether the thermal conductivity of a buried substrate is measurable within acceptable limits of uncertainty, sensitivity calculations provide the best means. The low modulation frequency of SSTTR enables it to measure the thermal conductivity of buried substrates that are traditionally challenging by TDTR and FDTR, demonstrated by presenting experimental data on three control samples. In addition, SSTTR has the capability to isolate the thermal properties of a buried film as long as the thermal resistance of this layer is much higher than those of the top thin film and substrate. This work marks an advancement in experimental metrology by establishing SSTTR as a robust technique for thermal characterizations of sub-surface buried substrates.

ACKNOWLEDGMENTS

The authors would like to acknowledge financial support from the U.S. Office of Naval Research under a MURI program (Grant No. N00014-18-1-2429). Z.C.L. acknowledges financial support from the Deanship of Scientific Research at the King Fahd University of Petroleum and Minerals under Project No. DF191001. J.K.H. acknowledges that the work at the Naval Research Laboratory (NRL) is supported by the Office of Naval Research.

DATA AVAILABILITY

The data that support the findings of this study are available from the corresponding author upon reasonable request.

REFERENCES

- ¹J.-S. Park, Y.-G. Mo, J.-K. Jeong, J.-H. Jeong, H.-S. Shin, and H.-J. Lee, "Thin film transistor and organic light-emitting display device having the thin film transistor," U.S. patent application 12/076, 216 (September 18, 2008).
- ²K. Tokunaga, "Thin film transistor and method of manufacturing thin film transistor," U.S. patent application 12/557, 212 (March 18, 2010).
- ³R. Venkatasubramanian, E. Siivola, T. Colpitts, and B. O'Quinn, "Thin-film thermoelectric devices with high room-temperature figures of merit," *Nature* **413**, 597–602 (2001).
- ⁴J.-Q. Xi, M. F. Schubert, J. K. Kim, E. F. Schubert, M. Chen, S.-Y. Lin, W. Liu, and J. A. Smart, "Optical thin-film materials with low refractive index for broadband elimination of Fresnel reflection," *Nat. Photonics* **1**, 176–179 (2007).
- ⁵P. Peumans, A. Yakimov, and S. R. Forrest, "Small molecular weight organic thin-film photodetectors and solar cells," *J. Appl. Phys.* **93**, 3693–3723 (2003).
- ⁶Y. Yang, L. Ma, and J. Wu, "Organic thin-film memory," *MRS Bull.* **29**, 833–837 (2004).
- ⁷S. H. Sung and B. W. Boudouris, "Systematic control of the nanostructure of semiconducting-ferroelectric polymer composites in thin film memory devices," *ACS Macro Lett.* **4**, 293–297 (2015).
- ⁸K. Aryana, J. T. Gaskins, J. Nag, D. A. Stewart, Z. Bai, S. Mukhopadhyay, J. C. Read, D. H. Olson, E. R. Hoglund, J. M. Howe *et al.*, "Interface controlled thermal resistances of ultra-thin chalcogenide-based phase change memory devices," *Nat. Commun.* **12**, 774 (2021).
- ⁹C. Dames, "Measuring the thermal conductivity of thin films: 3 omega and related electrothermal methods," *Annu. Rev. Heat Transfer* **16**, 7 (2013).
- ¹⁰D. G. Cahill, "Analysis of heat flow in layered structures for time-domain thermoreflectance," *Rev. Sci. Instrum.* **75**, 5119–5122 (2004).
- ¹¹A. J. Schmidt, X. Chen, and G. Chen, "Pulse accumulation, radial heat conduction, and anisotropic thermal conductivity in pump-probe transient thermoreflectance," *Rev. Sci. Instrum.* **79**, 114902 (2008).
- ¹²J. P. Feser, J. Liu, and D. G. Cahill, "Pump-probe measurements of the thermal conductivity tensor for materials lacking in-plane symmetry," *Rev. Sci. Instrum.* **85**, 104903 (2014).
- ¹³P. Jiang, X. Qian, and R. Yang, "Tutorial: Time-domain thermoreflectance (TDTR) for thermal property characterization of bulk and thin film materials," *J. Appl. Phys.* **124**, 161103 (2018).
- ¹⁴A. J. Schmidt, R. Cheaito, and M. Chiesa, "A frequency-domain thermoreflectance method for the characterization of thermal properties," *Rev. Sci. Instrum.* **80**, 094901 (2009).
- ¹⁵T. Borca-Tasciuc, A. R. Kumar, and G. Chen, "Data reduction in 3omega method for thin-film thermal conductivity determination," *Rev. Sci. Instrum.* **72**, 2139–2147 (2001).
- ¹⁶T. Tong and A. Majumdar, "Reexamining the 3-omega technique for thin film thermal characterization," *Rev. Sci. Instrum.* **77**, 104902 (2006).
- ¹⁷D. Zhao, X. Qian, X. Gu, S. A. Jajja, and R. Yang, "Measurement techniques for thermal conductivity and interfacial thermal conductance of bulk and thin film materials," *J. Electron. Packag.* **138**, 040802 (2016).
- ¹⁸J. Zhu, D. Tang, W. Wang, J. Liu, K. W. Holub, and R. Yang, "Ultrafast thermoreflectance techniques for measuring thermal conductivity and interface thermal conductance of thin films," *J. Appl. Phys.* **108**, 094315 (2010).
- ¹⁹J. L. Braun, D. H. Olson, J. T. Gaskins, and P. E. Hopkins, "A steady-state thermoreflectance method to measure thermal conductivity," *Rev. Sci. Instrum.* **90**, 024905 (2019).
- ²⁰P. Jiang, X. Qian, and R. Yang, "Time-domain thermoreflectance (TDTR) measurements of anisotropic thermal conductivity using a variable spot size approach," *Rev. Sci. Instrum.* **88**, 074901 (2017).
- ²¹L. Tang and C. Dames, "Anisotropic thermal conductivity tensor measurements using beam-offset frequency domain thermoreflectance (BO-FDTR) for materials lacking in-plane symmetry," *Int. J. Heat Mass Transfer* **164**, 120600 (2021).
- ²²Y. R. Koh, Z. Cheng, A. Mamun, M. S. B. Hoque, Z. Liu, T. Bai, K. Hussain, M. E. Liao, R. Li, J. T. Gaskins *et al.*, "Bulk-like intrinsic phonon thermal conductivity of micrometer thick aln films," *ACS Appl. Mater. Interfaces* **12**, 29443–29450 (2020).

- ²³B. Chatterjee, D. Shoemaker, Y. Song, T. Shi, H.-L. Huang, D. Keum, A. Krishnan, B. M. Foley, I. Jovanovic, J. Hwang *et al.*, "Cumulative impacts of proton irradiation on the self-heating of AlGaIn/GaN HEMTs," *ACS Appl. Electron. Mater.* **2**, 980–991 (2020).
- ²⁴R. Rosei and D. W. Lynch, "Thermomodulation spectra of Al, Au, and Cu," *Phys. Rev. B* **5**, 3883 (1972).
- ²⁵Y. K. Koh and D. G. Cahill, "Frequency dependence of the thermal conductivity of semiconductor alloys," *Phys. Rev. B* **76**, 075207 (2007).
- ²⁶J. L. Braun and P. E. Hopkins, "Upper limit to the thermal penetration depth during modulated heating of multilayer thin films with pulsed and continuous wave lasers: A numerical study," *J. Appl. Phys.* **121**, 175107 (2017).
- ²⁷J. L. Braun, C. J. Szejewski, A. Giri, and P. E. Hopkins, "On the steady-state temperature rise during laser heating of multilayer thin films in optical pump-probe techniques," *J. Heat Transfer* **140**, 052801 (2018).
- ²⁸D. H. Olson, J. L. Braun, and P. E. Hopkins, "Spatially resolved thermoreflectance techniques for thermal conductivity measurements from the nanoscale to the mesoscale," *J. Appl. Phys.* **126**, 150901 (2019).
- ²⁹R. B. Wilson, B. A. Apgar, L. W. Martin, and D. G. Cahill, "Thermoreflectance of metal transducers for optical pump-probe studies of thermal properties," *Opt. Express* **20**, 28829–28838 (2012).
- ³⁰Y. Wang, J. Y. Park, Y. K. Koh, and D. G. Cahill, "Thermoreflectance of metal transducers for time-domain thermoreflectance," *J. Appl. Phys.* **108**, 043507 (2010).
- ³¹C. M. Rost, J. Braun, K. Ferri, L. Backman, A. Giri, E. J. Opila, J.-P. Maria, and P. E. Hopkins, "Hafnium nitride films for thermoreflectance transducers at high temperatures: Potential based on heating from laser absorption," *Appl. Phys. Lett.* **111**, 151902 (2017).
- ³²L. Wang, R. Cheaito, J. L. Braun, A. Giri, and P. E. Hopkins, "Thermal conductivity measurements of non-metals via combined time- and frequency-domain thermoreflectance without a metal film transducer," *Rev. Sci. Instrum.* **87**, 094902 (2016).
- ³³E. L. Radue, J. A. Tomko, A. Giri, J. L. Braun, X. Zhou, O. V. Prezhdo, E. L. Runnerstrom, J.-P. Maria, and P. E. Hopkins, "Hot electron thermoreflectance coefficient of gold during electron-phonon nonequilibrium," *ACS Photonics* **5**, 4880–4887 (2018).
- ³⁴M. Qin, J. Gild, C. Hu, H. Wang, M. S. B. Hoque, J. L. Braun, T. J. Harrington, P. E. Hopkins, K. S. Vecchio, and J. Luo, "Dual-phase high-entropy ultrahigh temperature ceramics," *J. Eur. Ceram. Soc.* **40**, 5037–5050 (2020).
- ³⁵E. Jang, P. Banerjee, J. Huang, R. Holley, J. T. Gaskins, M. S. B. Hoque, P. E. Hopkins *et al.*, "Thermoelectric performance enhancement of naturally occurring Bi and chitosan composite films using energy efficient method," *Electronics* **9**, 532 (2020).
- ³⁶M. S. B. Hoque, Y. R. Koh, J. L. Braun, A. Mamun, Z. Liu, K. Huynh, M. E. Liao, K. Hussain, Z. Cheng, E. R. Hoglund *et al.*, "High in-plane thermal conductivity of aluminum nitride thin films," *ACS Nano* **15**, 9588–9599 (2021).
- ³⁷K. Ye, S. C. Siah, P. T. Erslev, A. Akey, C. Settens, M. S. B. Hoque, J. Braun, P. Hopkins, G. Teeter, T. Buonassisi *et al.*, "Tuning electrical, optical, and thermal properties through cation disorder in $\text{Cu}_2\text{ZnSnS}_4$," *Chem. Mater.* **31**, 8402–8412 (2019).
- ³⁸A. Giri, A. Z. Chen, A. Mattoni, K. Aryana, D. Zhang, X. Hu, S.-H. Lee, J. J. Choi, and P. E. Hopkins, "Ultralow thermal conductivity of two-dimensional metal halide perovskites," *Nano Lett.* **20**, 3331–3337 (2020).
- ³⁹E. Ziade, J. Yang, G. Brummer, D. Nothern, T. Moustakas, and A. J. Schmidt, "Thermal transport through GaN–SiC interfaces from 300 to 600 K," *Appl. Phys. Lett.* **107**, 091605 (2015).
- ⁴⁰J. L. Braun, C. H. Baker, A. Giri, M. Elahi, K. Artyushkova, T. E. Beechem, P. M. Norris, Z. C. Leseman, J. T. Gaskins, and P. E. Hopkins, "Size effects on the thermal conductivity of amorphous silicon thin films," *Phys. Rev. B* **93**, 140201 (2016).
- ⁴¹M. S. Tareq, S. Zainuddin, E. Woodside, and F. Syed, "Investigation of the flexural and thermomechanical properties of nanoclay/graphene reinforced carbon fiber epoxy composites," *J. Mater. Res.* **34**, 3678–3687 (2019).
- ⁴²Z. Cheng, F. Mu, L. Yates, T. Suga, and S. Graham, "Interfacial thermal conductance across room-temperature-bonded GaN/diamond interfaces for GaN-on-diamond devices," *ACS Appl. Mater. Interfaces* **12**, 8376–8384 (2020).
- ⁴³A. Giri and P. E. Hopkins, "A review of experimental and computational advances in thermal boundary conductance and nanoscale thermal transport across solid interfaces," *Adv. Funct. Mater.* **30**, 1903857 (2020).
- ⁴⁴W. Fulkerson, J. P. Moore, R. K. Williams, R. S. Graves, and D. L. McElroy, "Thermal conductivity, electrical resistivity, and Seebeck coefficient of silicon from 100 to 1300 K," *Phys. Rev.* **167**, 765 (1968).
- ⁴⁵R. K. Kremer, K. Graf, M. Cardona, G. G. Devyatikh, A. V. Gusev, A. M. Gibin, A. V. Inyushkin, A. N. Taldenkov, and H.-J. Pohl, "Thermal conductivity of isotopically enriched ^{28}Si : Revisited," *Solid State Commun.* **131**, 499–503 (2004).
- ⁴⁶R. B. Wilson and D. G. Cahill, "Anisotropic failure of Fourier theory in time-domain thermoreflectance experiments," *Nat. Commun.* **5**, 5075 (2014).
- ⁴⁷T. E. Beechem, A. E. McDonald, E. J. Fuller, A. A. Talin, C. M. Rost, J.-P. Maria, J. T. Gaskins, P. E. Hopkins, and A. A. Allerman, "Size dictated thermal conductivity of GaN," *J. Appl. Phys.* **120**, 095104 (2016).
- ⁴⁸E. Ziade, J. Yang, G. Brummer, D. Nothern, T. Moustakas, and A. J. Schmidt, "Thickness dependent thermal conductivity of gallium nitride," *Appl. Phys. Lett.* **110**, 031903 (2017).
- ⁴⁹F. Mu, Z. Cheng, J. Shi, S. Shin, B. Xu, J. Shiomi, S. Graham, and T. Suga, "High thermal boundary conductance across bonded heterogeneous GaN–SiC interfaces," *ACS Appl. Mater. Interfaces* **11**, 33428–33434 (2019).
- ⁵⁰Q. Zheng, C. Li, A. Rai, J. H. Leach, D. A. Broido, and D. G. Cahill, "Thermal conductivity of GaN, ^{71}GaN , and SiC from 150 K to 850 K," *Phys. Rev. Mater.* **3**, 014601 (2019).
- ⁵¹H. Li, R. Hanus, C. A. Polanco, A. Zeidler, G. Koblmüller, Y. K. Koh, and L. Lindsay, "GaN thermal transport limited by the interplay of dislocations and size effects," *Phys. Rev. B* **102**, 014313 (2020).
- ⁵²L. Lindsay, D. A. Broido, and T. L. Reinecke, "Thermal conductivity and large isotope effect in GaN from first principles," *Phys. Rev. Lett.* **109**, 095901 (2012).
- ⁵³D. I. Florescu, V. M. Asnin, F. H. Pollak, R. J. Molnar, and C. E. C. Wood, "High spatial resolution thermal conductivity and Raman spectroscopy investigation of hydride vapor phase epitaxy grown n -GaN/sapphire (0001): Doping dependence," *J. Appl. Phys.* **88**, 3295–3300 (2000).
- ⁵⁴D. G. Cahill, S.-M. Lee, and T. I. Selinder, "Thermal conductivity of κ - Al_2O_3 and α - Al_2O_3 wear-resistant coatings," *J. Appl. Phys.* **83**, 5783–5786 (1998).
- ⁵⁵L. Lindsay, D. A. Broido, and T. L. Reinecke, "Ab initio thermal transport in compound semiconductors," *Phys. Rev. B* **87**, 165201 (2013).
- ⁵⁶R. B. Wilson and D. G. Cahill, "Limits to Fourier theory in high thermal conductivity single crystals," *Appl. Phys. Lett.* **107**, 203112 (2015).
- ⁵⁷W. Zheng, B. Huang, and Y. K. Koh, "Ultralow thermal conductivity and thermal diffusivity of graphene/metal heterostructures through scarcity of low-energy modes in graphene," *ACS Appl. Mater. Interfaces* **12**, 9572–9579 (2020).
- ⁵⁸Y. R. Koh, J. Shi, B. Wang, R. Hu, H. Ahmad, S. Kerdsonpanya, E. Milosevic, W. A. Doolittle, D. Gall, Z. Tian *et al.*, "Thermal boundary conductance across epitaxial metal/sapphire interfaces," *Phys. Rev. B* **102**, 205304 (2020).
- ⁵⁹D. H. Olson, J. T. Gaskins, J. A. Tomko, E. J. Opila, R. A. Golden, G. J. K. Harrington, A. L. Chamberlain, and P. E. Hopkins, "Local thermal conductivity measurements to determine the fraction of α -cristobalite in thermally grown oxides for aerospace applications," *Scr. Mater.* **177**, 214–217 (2020).
- ⁶⁰Y. Dong, B.-Y. Cao, and Z.-Y. Guo, "Ballistic-diffusive phonon transport and size induced anisotropy of thermal conductivity of silicon nanofilms," *Physica E* **66**, 1–6 (2015).
- ⁶¹D. G. Cahill, "Thermal conductivity measurement from 30 to 750 K: The 3ω method," *Rev. Sci. Instrum.* **61**, 802–808 (1990).